Energy Evolution and Water Immersion-Induced Weakening Mechanism in the Sandstone Roof of Coal Mines

Wenjie Liu
Anhui University of Science and Technology
Ke Yang (keyang2003@163.com)
Anhui University of Science and Technology https://orcid.org/0000-0002-6931-5946
Shuai Zhang
China University of Mining and Technology
Zhainan Zhang
Anhui University of Science and Technology
Rijie Xu
Anhui University of Science and Technology

Research

Keywords: Mining engineering, energy evolution, water-rock interaction, weakening mechanism

Posted Date: October 12th, 2021

DOI: https://doi.org/10.21203/rs.3.rs-955141/v1

Energy Evolution and Water Immersion-Induced Weakening Mechanism in the Sandstone Roof of Coal Mines

Wenjie Liu[1,3,4], Ke Yang[1,2,3,4], Shuai Zhang[5], Zhainan Zhang [1,3,4], Rijie Xu [1,3,4]

[1]State Key Laboratory of Mining Response and Disaster Prevention and Control in Deep Coal Mines, Anhui University of Science and Technology, Huainan 232001, China

[2]Institute of Energy, Hefei Comprehensive National Science Center, Anhui, Hefei, 230031, China;

[3]National & Local Joint Engineering Research Center of precision coal mining, Anhui University of Science and Technology, Anhui, Huainan, 232001, China

[4]Key Laboratory of Mining Coal Safety and Efficiently Constructed by Anhui Province and Ministry of Education, Anhui University of Science and Technology, Huainan 232001, China

[5]State Key Laboratory of Coal Resources and Safe Mining, China University of Mining and Technology, Xuzhou, Jiangsu 221116, China

Abstract The instability of underground spaces in abandoned coal mines with water-immersed rocks is one of the main hazards hindering the geothermal energy utilization and ecological restoration of post-mining areas. This study conducted graded cyclic loading-unloading tests of five groups of sandstone samples with different water contents. The evolution laws of input, elastic, dissipated, damping, and plastic energies were explored in detail, taking into account the damping effect. The normalized plastic energy was used to characterize the damage evolution of sandstone samples, which failure modes were analyzed from both macroscopic and microscopic perspectives. The X-ray diffraction technique and scanning electron microscopy were used to reveal the softening mechanism of sandstone's strength and elastic energy storage limit. The results showed that the graded cyclic loading's input, elastic, and dissipated energies increased gradually. The elastic energy share first increased and then stabilized, while dissipated energy share variation had the opposite trend. In each cycle, the input energy was primarily stored in the form of elastic energy, while the dissipated energy was mainly used to overcome the damping of sandstone. When the normalized number of cycles approached unity, the plastic energy share sharply increased, while that of the dampening energy featured an abrupt drop. Such change indicated an inevitable instability failure of the water-bearing sandstone. As the water content increased, the pore water exhibited more substantial lubrication, water-wedging, and dissolution effects on mineral particles. As a result, the latter obtained a round form, and the elastic energy storage limit of the sandstone decreased. When the water content was increased, the damage factor of sandstone after the same number of cycles increased at a relatively higher rate, and there was a transition of failure mode from brittle to ductile.

Keywords: Mining engineering; energy evolution; water-rock interaction; weakening mechanism

1 Introduction

After the closure of coal mines due to low economic benefit or resource exhaustion, the surface water and the groundwater contained in the aquifer will rapidly fill underground spaces through the fissured zone, causing the groundwater level drop, water pollution, surface subsidence, changes in the geological environment, and secondary disasters (Li et al. 2019). Within the framework of clean energy production and ecological restoration of the post-mining areas, considerable efforts have been made worldwide on utilizing geothermal energy, water,

*Corresponding author: Ke Yang Email:keyang2003@163.com

and spaces in abandoned coal mines. For example, some scholars have suggested constructing underground reservoirs of abandoned coal mines (Bian et al. 2021; Gu et al. 2015), developing geothermal resources (Pu et al. 2021; Jardon et al. 2013), and building pumped storage power stations (Fan et al. 2020; Xie et al. 2020).

Complex water-rock interactions, physical effects, and chemical reactions commonly occur in abandoned coal mines due to tidal action and water erosion, significantly deteriorating rock stability and residual strength. This issue was addressed by numerous scholars, who investigated the mechanical characteristics and failure mechanism of water-bearing rocks (Wong et al. 2016; Hashiba et al. 2015) and conducted post-peak cyclic loading-unloading tests for coarse sandstone in natural and water-saturated conditions (Niu et al. 2018). The latter found that the water-saturated coarse sandstone exhibited a more significant increase in lateral and volumetric strains compared with the natural condition. In uniaxial loading-unloading tests, water saturation had an apparent softening effect on post-peak fractured coarse sandstone strength and elastic modulus. Zhou et al. (2016) conducted static and dynamic mechanical tests of sandstone samples with different water contents under the dry-wet cycles. They found that water-bearing sandstone could gradually restore its mechanical characteristics in dry conditions. The tensile strengths of sandstone with the same water contents were different under drying and water-immersion conditions. Hua et al. (2019) compared the mechanical fracture characteristics of sandstone under dry-wet cycling and long-term water immersion. They reported that dry-wet cycling caused a more significant sandstone fracture performance deterioration than long-term water immersion. Rock damage and failure were closely related to energy accumulation, dissipation, and release. Therefore, some scholars have analyzed the impact of water on rocks from an energy perspective (Li et al. 2015; Wang et al. 2017). Chen et al. (2019) pointed out that the amount of energy released at the sandstone's compaction and elastic deformation stages increased significantly. The water content increased, and the amount of energy released after failure decreased. A higher water content led to a reduction of sandstone's brittleness and enhanced its plastic deformation. Geng et al. (2020) conducted uniaxial compression tests on dry, water-bearing, and saturated sandstone samples. Their results showed that the water-softened sandstone was more prone to ductile damage and released less elastic energy. Ma et al. (2018) carried out uniaxial compressing testing of gypsum rocks under different durations of water immersion. The results showed that gypsum rocks' input, elastic, and dissipated energies decreased as the water immersion was prolonged. They further described the damage characteristics of gypsum rock subjected to the water-weakening effect and uniaxial loading via a constitutive damage model based on energy dissipation.

As shown above, the mechanical characteristics, energy evolution, and failure modes of water-bearing sandstone during its deformation and failure processes have been extensively studied. However, the studies on the evolution law of residual plastic strain in sandstone with different water contents under graded cyclic loading are quite scarce. Besides, the aspects of the hysteresis effect of rocks and the energy dissipated by damping were rarely considered. The present study performed the uniaxial loading and cyclic loading-unloading tests of sandstone samples with different water contents. The mechanical response of sandstone samples with different water contents under graded cyclic loading-unloading was determined. Considering the viscoelastic properties of sandstone, the evolution laws of damping and dissipated energies were determined. The damage evolution of sandstone

during the deformation and failure process was also quantitatively described based on the energy principle. The macroscopic crack propagation process of sandstone samples was monitored using digital speckle technology. SEM was performed to observe the microstructure of fractured sandstone samples. Finally, the mechanism by which water immersion weakened the mechanical properties of the sandstone was revealed. The research findings offer theoretical support for engineering safety and stability evaluation of rocks in coal mine underground reservoirs.

2 Experimental Setup and Test Scheme

2.1 Sample preparation

The sandstone samples were collected from the roof of the 4# coal seam of the Panbei Coal Mine in Huainan and Huaibei Mining Area, China. Unweathered sandstone samples with good integrity and uniform texture were sealed in wax at the collection site and transported to the laboratory. According to the International Society for Rock Mechanics and Rock Engineering (ISRM) requirements, the sandstone was cut, drilled, and polished into standard cylindrical samples with a diameter of 50mm and length of 100mm. Thirty standard samples were subdivided into five groups and prepared for tests. Before the mechanical tests, the sandstone samples were dried at 105℃ in an oven for 24h until a constant weight was achieved. Then, samples of each group were taken out and placed into distilled water for non-invasive natural water immersion tests (Yu et al. 2019), providing five levels of the water content (from dry to saturated): 0% (dry), 0.50%, 1.01%, 1.52%, and 2.07%. Each sandstone sample was weighed before and after each experimental step. According to formula (1), the natural water content of the sandstone samples was calculated to be approximately 0.3%; the water content of the water-saturated sandstone sample was about 2.07%.

$$W=(M_w-M_0)/M_0\times100\% \quad (1)$$

where W is water content in %, while M_w and M_0 are masses of wetted and dry sandstone samples, respectively.

As shown in Fig. 1, five levels of the water content of sandstone samples were set up: 0, 0.50, 1.01, 1.52, and 2.07%. Uniaxial compression and uniaxial graded cyclic loading-unloading tests were performed for the sandstone samples. Given the effect of environmental factors on the experimental results, tests were performed immediately after each group of samples was prepared.

2.2 Test system

As shown in Fig.2, the test system mainly consisted of a rock mechanical testing module, a digital video acquisition module, an SEM testing module, and an XRD testing module. The rock mechanical testing module was an RMT-150B multifunction automatic rigid rock servo material testing machine, which could perform conventional uniaxial and triaxial compression tests with high precision. The maximal axial load imposed by this machine was 1000 kN, with a loading rate of 0.01-100 kN/s. The measuring range of the axial displacement sensor was 0-5 mm, with a resolution of 0.0015 m, which satisfied the test requirements. The SEM testing module was a FLEXSEM 1000, a compact SEM, for high-resolution observation in a low-vacuum mode. The magnification factor ranged from 60,000 to 300,000, with an accelerating voltage of 0.3-20 kV and a resolution of 4 nm. The XRD testing module was a SmartLab X-ray diffractometer for analyzing the mineral composition of the sandstone samples. The digital video acquisition module was a Nikon digital camera, which captured the fracture morphology of the sandstone samples during the loading process.

2.3 Experimental scheme and results

Each group of the sandstone samples was further split into subgroups D and X, which were used for the uniaxial compression and uniaxial graded loading-unloading tests, respectively. To improve the experimental accuracy and reduce the randomness of the experimental results, no less than three parallel tests were conducted for each loading scheme and each water content. The uniaxial compression tests were first conducted to obtain the strain-stress curves for different water contents, as shown in Fig. 3. Then, the axial pressure at each unloading point was determined to design the subsequent cyclic loading-unloading test. The stress-controlled mode was implemented in the uniaxial cyclic loading-unloading tests, as shown in Fig.4.

The loading and unloading rates were both 0.5 MPa/s. The stress gradient at the loading stage was 5 MPa. The target value of unloading for the unloading stage was set to 1.25 MPa. The stress path of the uniaxial cyclic loading-unloading test was as follows: 0, 5, 1.25, 10, 1.25, 15, 1.25, 20, 1.25, 25, 1.25, 30MPa, sample failure, test termination. To facilitate the analysis of the test results, water content normalization was performed. The saturated water content was designated as 100%. Then, the samples in each group were numbered. For example, X-25%-1 represented the uniaxial graded cyclic loading-unloading test for the first group of samples with a water content of 0.50%. D-75%-3 represented the uniaxial compression testing of the third group of samples with a water content of 1.52%.

Figure 5 shows the XRD results on the mineral composition of the three groups of sandstone samples with different water contents. The sandstone samples were composed of mineral crystals, including quartz, kaolinite, albite, and calcite. The quartz content was the highest among all minerals in the three groups of samples, accounting for about 50%. The sandstone samples with different water contents varied in mineral composition and content. The sandstone samples with a zero water content were mainly composed of two minerals. Those with a water content of 2.07% were mainly composed of three minerals. Changes in mineral content and composition did not significantly correlate with the water content.

3. Analysis of Mechanical Characteristics of Sandstone Samples under Cyclic Loading

The softening coefficient was used to characterize the softening properties of sandstone samples with different water contents more intuitively. The softening coefficient λ was defined as the ratio of the compressive strength R_w of the water-bearing sandstone samples with different water contents to the compressive strength R_d of the dry sandstone, according to the following formula:

$$\lambda = \frac{R_w}{R_d}; 0 < \lambda \le 1 \tag{2}$$

The smaller the softening coefficient, the stronger the softening and the greater the impact of water on the rocks. As shown in Table 1, water had a significant impact on the mechanical properties of sandstone. Compared with dry samples, the uniaxial compressive strength of water-bearing sandstone significantly dropped from the initial 114.09 to 16.39MPa with the water content. The elastic modulus of the sandstone also decreased continuously from 19.70 to 3.47GPa, as the water content increased. On the contrary, Poisson's ratio increased.

Figure 6 shows the stress-strain curves of different groups of sandstone samples subjected to graded cyclic loading-unloading tests. All sandstone samples underwent recoverable plastic deformation during each loading-unloading cycle and unrecoverable plastic deformation. Before the failure, the stress-strain curve deviated from the historical stress-strain curve. Besides, as the irreversible plastic deformation accumulated, the cyclic loading-unloading curve gradually shifted toward larger strain values. Under graded cyclic loading-unloading, the sandstone strength and the number of loading-unloading cycles to failure gradually decreased as the water content increased.The stress path of a single loading-unloading cycle was analyzed separately, as shown in Fig. 7. In Fig.7, point *O* is the starting point of the $i^{\text{-th}}$ cyclic loading curve; point *A* is the end point of the $i^{\text{-th}}$ cyclic loading curve and the starting point of the $i^{\text{-th}}$ cyclic unloading curve; point *B* is the point of intersection between the $i^{\text{-th}}$ cyclic unloading curve and the i+1$^{\text{-th}}$ cyclic loading curve; point *C* is the end point of the $i^{\text{-th}}$ cyclic unloading curve and the start point of the i+1$^{\text{-th}}$ cyclic loading curve; ε_o, ε_A, ε_B, and ε_C are the strain values of the corresponding coordinates, respectively; σ_A and σ_B are the stress values of the corresponding coordinates, respectively. The cyclic elastic strain ε_{ei} for the $i^{\text{-th}}$ cycle is defined as the difference between the peak strain ε_A of the $i^{\text{-th}}$ cycle and the residual plastic strain ε_C of the $i^{\text{-th}}$ cycle; the residual plastic strain ε_{pi} is the difference between the strain ε_o at the starting point of the loading curve of the $i^{\text{-th}}$ cycle (point *O*) and the strain ε_c at the end point of the unloading curve of the $i^{\text{-th}}$ cycle.

For the sake of convenience, the number of cycles to failure was normalized. Figure 8 shows the curves of elastic strain ε_{ei} or residual plastic strain ε_{pi} versus the normalized number of cycles.

As shown in Fig.8, the sandstone underwent plastic strain and residual plastic strain in each cycle. Since the rocks were inhomogeneous anisotropic materials, the primary pores and cracks within the sandstone were gradually compacted under initial cyclic loading. At this stage, the plastic strain curve versus the normalized number of cycles showed a non-linear increasing trend, and the residual plastic strain was large. The sandstone entered the plastic deformation stage in the subsequent cycles as the number of cycles and stress increased. The curve of the elastic strain versus the normalized number of cycles showed an approximately linear increasing trend. At this stage, the residual plastic strain decreased rapidly and stabilized. When the residual strain accumulated to a certain level, the microcracks within the sandstone became interconnected and penetrated the samples. The curve of residual plastic strain versus the normalized number of cycles showed a minor increase.

4. Energy Evolution Analysis

4.1 Energy conversion theory considering viscoelastic deformation

Under cyclic loading, the entire process of sandstone deformation and failure was accompanied by energy accumulation, release, and dissipation. According to the first law of thermodynamics, it was assumed that the sandstone was not engaged in thermal exchange with the environment during deformation and failure, and the radiant energy and the energy of the acoustic emission were neglected. Then, the work done by the press machine to the sandstone samples was the total input energy. As shown in Fig. 6, the energy value for each cycle can be calculated by Eqs.(3)-(6), according to Xie et al. (2005):

$$U_i = U_{ei} + U_{disi} \tag{3}$$

$$U_i = \int_{\varepsilon_o}^{\varepsilon_A} \sigma_i^+ d\varepsilon_i \quad (4)$$

$$U_{ei} = \int_{\varepsilon_c}^{\varepsilon_A} \sigma_i^- d\varepsilon_i \quad (5)$$

$$U_{\mathrm{dis}i} = U_i - U_{ei} = \int_{\varepsilon_o}^{\varepsilon_A} \sigma_i^+ d\varepsilon_i - \int_{\varepsilon_c}^{\varepsilon_A} \sigma_i^- d\varepsilon_i \quad (6)$$

where U_i, U_{ei}, and U_{disi} are the input, elastic, and dissipated energies of the i-th cycle, respectively; σ_i^+ and σ_{i+1}^+ are the stresses imposed upon the i-th and the i+1-th loading, respectively; σ_i^- is the stress imposed upon the i-th unloading.

Rocks are aggregates of mineral particles with complex mineral composition and structure, which implies their significant heterogeneity and anisotropy. In most studies on the energy evolution law of rocks under graded cyclic loading-unloading, rocks were treated as elastoplastic materials. The area enclosed by the cyclic loading-unloading curve and the coordinate axis (U_{disi}) was treated as the magnitude of energy causing rock damage and failure. However, such an assumption neglected the viscous friction between mineral particles and the liquid. For this reason, the plastic energy causing rock damage was not differentiated from the damping energy spent on overcoming the viscous friction. In the present study, we considered the viscoelastic deformation of the sand-bearing sandstone. For each cyclic loading, the dissipated energy U_{disi} was split into plastic energy U_{pi} and damping energy U_{dami}. We assumed that damping did not cause sandstone damage and failure, and the plastic energy promoted the plastic deformation of rocks as an energy causing strength weakening of the sandstone.

As shown in Fig. 7, the physical meaning of point B was approximately the stress state during the i-th loading-unloading cycle. Unloading started from this stress state, followed by another loading. Then, the sandstone returned to the initial stress state, thus forming a closed hysteresis loop BCB. For a rock treated as an elastoplastic material, the shape of the hysteresis loop under elastoplastic deformation is jointly determined by rock viscosity and plasticity. Rock as an elastoplastic material undergoes no plastic deformation, and its unloading path differs. Nevertheless, a closed hysteresis loop can still be formed for the rock. Stevens et al. (1980) and Kuwahara et al. (1990) found that under the loading-unloading action, many new microcracks would appear in rocks only when the stress during the second loading exceeded the peak stress upon the first loading. It was believed that during the uniaxial graded loading-unloading, no new cracks were generated in the rocks if the loading stress was lower than the stress imposed during the previous loading. Hence, there would be no growth in plastic energy. Based on the above, we assumed that the sandstone was an elastoplastic material along the stress path from point B to point C upon unloading and back to point B upon loading. At this stage, the sandstone underwent elastoplastic deformation, and the elastic energy was not dissipated. The energy lost during this cycle was the work done by damping that arose from rock viscosity.

Similarly, we assumed that the sandstone was not engaged in thermal exchange with the environment. Thermal radiation and acoustic emission energy were neglected. Thus, the area of the hysteresis loop BCB was the energy dissipated by overcoming the viscous friction between the mineral particles and liquid, i.e., the damping energy U_{dami}. The dissipated energy U_{di} minus this portion of the damping energy was the plastic energy U_{pi} causing rock damage. The relationship between these energies and their magnitude can be calculated using Eqs. (7)-(9):

$$U_{\mathrm{dis}i} = U_{p_i} + U_{dami} \quad (7)$$

$$U_{dami} = \int_{\varepsilon_o}^{\varepsilon_B} (\sigma_{i+1}^+ - \sigma_i^+) d\varepsilon_i \quad (8)$$

$$U_{pi} = \int_{\varepsilon_o}^{\varepsilon_A} \sigma_i^+ d\varepsilon_i - \int_{\varepsilon_C}^{\varepsilon_A} \sigma_i^- d\varepsilon_i - \int_{\varepsilon_o}^{\varepsilon_B} (\sigma_{i+1}^+ - \sigma_i^+) d\varepsilon_i \qquad (9)$$

4.2 Energy evolution law

According to theoretical background and formulas (3)-(6) described in section 4.1, the evolution laws of the elastic and dissipated energies were derived, and their shares in sandstone samples with different water contents were calculated and plotted in Fig. 9.It can be seen from Fig.9 that:

(1) The input, elastic, and dissipated energies of sandstone samples with different water contents increased with the normalized number of cycles. This was because a larger normalized number of cycles implied a larger work on the sandstone sample exerted by the external force. As a result, the input energy increased. Part of the input energy was stored in the sandstone in the form of elastic energy. The remaining part was dissipated by causing rock damage.

(2) The elastic energy and dissipated energy shares were compared under different water contents. Under the initial cyclic loading, the input energy was mainly in the form of dissipated energy. The dissipated energy share significantly exceeded that of the elastic energy. Under initial loading, the sandstone underwent damage and failure caused by the compression of primary defects, leading to more significant energy dissipation. Besides, the larger the water content, the higher the dissipated energy share and the more severe the sandstone damage under initial loading.

(3) As the normalized number of cycles increased, the elastic energy share gradually increased, and that of the dissipated energy decreased and finally stabilized. These results indicated that the input energy was stored in the sandstone mainly in the form of elastic energy at this stage. The elastic energy share ranged from 0.7 to 0.9. Besides, the greater the water content, the smaller the elastic energy share, and the more severe the sample damage under the same stress.

(4) When the normalized number of cycles approached unity, the input, elastic, and dissipated energies still kept increasing. The elastic energy share decreased, and that of the dissipated energy increased. This indicated that the microcracks within the sandstone gradually propagated and penetrated the sandstone sample, resulting in its failure. Given the above, it was feasible to predict the sandstone failure based on the energy evolution law.

Using formulas (7)-(9), we calculated the evolution law of the damping energy, plastic energy, and their shares in sandstone samples with different water contents. The results are shown in Fig. 10.

It can be found from Fig.10 that as the normalized number of cycles increased, the damping energy and the plastic energy of the sandstone with different water contents increased gradually. The plastic energy share first decreased rapidly, then stabilized, and later increased abruptly. The damping energy share showed the opposite trend. Such variation was considered relevant to rock compression and peak damage. The analysis of dissipated energy shares in the sandstone samples with different water contents revealed that they decreased with water content. The majority of the dissipated energy in each cycle was spent on overcoming the work done by viscosity. As the water content increased, the plastic energy share became gradually larger than that of the damping energy. This indicated that water immersion significantly reduced the work done by the frictional damping between the mineral particles. As a result, the bonding strength between the mineral particles was attenuated, promoting sandstone damage and failure. The variation of the elastic energy share was similar to that of dissipated energy. When the normalized number of cycles approached unity, the plastic energy share increased abruptly. In contrast, the damping energy share sharply dropped, portending the impending failure of the sandstone sample.

4.2 Damage mechanism based on plastic energy

According to the above findings, the input energy under cyclic loading-unloading conditions was stored or released mainly in the form of elastic energy or dissipated in the form of damping energy. Only a small share of the input energy was spent on sandstone damage and failure. Besides, the higher the water content, the larger the plastic energy share under the same stress gradient. To characterize the degree of rock damage and failure, Liu et al. (2018) performed normalization of the dissipated energy. They analyzed the cumulative damage law of rocks under cyclic loading. Plastic energy was a primary factor causing rock damage, while the damping energy did not lead to residual deformation and damage. Therefore, it was considered more accurate and reasonable to use normalized plastic energy to characterize rock damage. The damage factor (D) was defined as the ratio of cumulative damage to total damage in the following equation:

$$D = \frac{\sum U_{pi}}{U_p} \tag{10}$$

where U_{pi} is the plastic energy generated during the $i^{\text{-th}}$ cycle, while U_p is the total plastic energy.

The damage variable estimated by this formula varied between zero and unity, satisfying the principle of damage irreversibility. Taking a dry sandstone sample (X-0) as an example, the damage factor evolution curve was plotted in Fig.11 and subdivided into three stages, which differed by the variation trend of damage factor, defined as the derivative of the damage factor concerning the number of cycles: decelerating growth, stable growth, and accelerating growth.

At the stage of decelerating growth, the damage factor grew at a saturating rate under the initial cyclic loading due to rock anisotropy and heterogeneity. The damage factor reached 35% at the stage of decelerating growth. At the stable growth stage, the damage generated per cycle gradually approached a constant value as the graded cyclic loading increased. This stage accounted for the largest majority of the loading-unloading cycles. The above results indicated that the damage accumulated stably, while microcracks initiated and propagated without coalescing and penetrated the samples' bulk. When the damage reached about 80%, its accumulation accelerated. The damage generated in the last 2-3 cycles accounted for nearly 24%, resulting in instability failure. These results indicated that as the test proceeded, the pores and cracks propagated and became interconnected. After the cracks propagated to a certain degree, crack development and damage accumulation were accelerated. As the water content increased, the curve of the damage factor versus the number of cycles shifted towards the Y-axis on the whole. The region corresponding to the decelerating growth stage gradually disappeared. This implied that under the graded cyclic loading conditions, a higher water content corresponded to faster growth of the damage factor. The presence of water accelerated sandstone damage. In the water-saturated sandstone sample (X-100), the damage generated in the first cycle accounted for about 34%.

5. Fracture Morphology and Failure Modes

Rock damage accumulation is the process whereby microcracks initiate, propagate, and become interconnected within the rocks. Fracture morphology characteristics vary at different stages of crack development. The fracture surface is where the microcracks and pores are found in large numbers. Microcracks and pores propagate along the weakest plane until the penetrating fracture surface is formed, leading to varying failure

modes in the sandstone. We studied the microscopic fracture characteristics of cracks along with the macroscopic failure morphology of sandstone. Therefore, the impact of water on the sandstone failure process was investigated on both microscopic and macroscopic scales. This approach was conducive to disclosing the macroscopic mechanical strength-weakening mechanism and the energy dissipation mechanism in water-bearing sandstone.

5.1 Fracture morphology

Flex SEM1000 was applied to observe the typical fracture in dry, semi-saturated, and saturated sandstone samples under grade cyclic loading-unloading. The microstructural changes of the sandstone samples under different magnification factors are shown in Fig. 12. According to the figure, the fractures were serrated in the dry sandstone samples, and the mineral particles had dense structures. The cementing materials between the particles were compacted. Some micro-pores and cracks were only found along the mineral particle boundaries and in the cementing materials. In the semi-saturated sandstone samples, the microstructure patterns varied significantly. Corrosion pits appeared on the particle surfaces. A large number of secondary minerals and residues adhered to the mineral particle surfaces. In saturated sandstone samples, the dissolution and corrosion of the calcareous cement were significant in loose structures. The cracks developed and propagated, and the mineral particles were more rounded. As analyzed above, the cementation degree decreased in sandstone due to water immersion. The frictional damping between the particles was weakened. Consequently, the sandstone samples gradually evolved from dense structures to loose ones. The water-rock interaction and the loading-unloading cycles promoted damage accumulation and microstructural changes in sandstone samples.

5.2 Failure mode

Along with the development of monitoring technologies, digital imaging methods became very instrumental in studying macroscopic crack propagation in rocks. The preparation of artificial speckles on the surface of the water-bearing sandstone samples would inevitably increase the test duration. To mitigate this problem, we used the PhotoInfor and PostViewer image analysis software packages to determine sandstone deformation and failure during the tests (Li et al. 2006). The displacement evolution law on the surface of sandstone samples with different water contents was obtained.

Figure 13 shows the cloud maps of displacement field at different time points for the corresponding number of cycles in dry, semi-saturated (water content 1.01%), and water-saturated sandstone samples under grade cyclic loading-unloading. According to Fig. 13 (a), cracks initiated from the upper and lower edges of the dry sandstone sample successively after twenty cycles. Later, the cracks propagated along the principal stress direction and developed into three tensile cracks growing parallel with the loading direction. The sandstone sample underwent splitting failure. According to Fig. 13 (b), cracks initiated from the upper right and the lower middle parts of the semi-saturated sandstone sample successively. The cracks first propagated along the loading direction and then merged into one crack. The sandstone samples had a failure of tensile-shear mixed mode. According to Fig. 13 (c), cracks initiated from the middle of the saturated sandstone sample and gradually propagated. One inclined crack was generated in the upper and lower parts of the sample, respectively. The sandstone sample had a single inclined plane shear failure mode.

As the water content increased, the failure mode changed from tensile-brittle cleavage fracture in the dry state to tensile-shear mixed-mode failure. In the water-saturated state, sandstone samples had a single shear failure with some ductile features. Meanwhile, more and more secondary fissures were generated near the main fracture,

resulting in increasingly complicated patterns in the displacement field cloud maps. The most probable reason was that the sandstone bulk was damaged due to the water's lubrication, wedging, and corrosion effects. As a result, a shear zone appeared. Besides, as the water content increased, the shear zone within the sample became increasingly prominent. The presence of the shear zone contributed to the shear slip failure of the sandstone samples under stress.

6. Discussion

According to the above analyses, the mechanical properties of sandstone samples permanently deteriorated as the water content increased, while their damage accumulated gradually. Both the compressive strength and the energy storage characteristics deteriorated significantly. The above phenomena were primarily attributed to physical interactions and chemical reactions between water and sandstone, which are briefly summarized below.

The coal measures is a lithostratigraphic term for the coal-bearing part of the Upper Carboniferous System, consisting of such rocks as claystone, shale, siltstone, sandstone, etc., interstratified with the beds of coal. Coal measures sandstone is a sedimentary rock composed of mineral particles of varying sizes and shapes. Such sandstone has many defects within, including microcracks, fissures, and pores. In water immersion tests, the water first fills the pores and fissures between the mineral particles rapidly. If the water immersion lasts for a long period, the pore water will gradually permeate to the mineral particle surfaces to form bound water there. Under the external force action, the sandstone samples undergo frictional slip between the mineral particles. As the bound water amount formed on the mineral particle surfaces increases, water's lubricating and softening effects are enhanced. The bonding strength between the particles is weakened. As a consequence, the frictional coefficient and the cohesive force within the sandstone decrease to varying extents.

According to SEM and XRD of typical fractures, the sandstone was mainly composed of quartz, feldspar, and clay minerals; on the microscopic scale, the fracture surface became rounded gradually. The cracks and fissures within the sandstone samples were the primary sites where the physical, chemical, and mechanical interactions occurred between water and rocks. As the water content increased, the calcareous cement was more likely to be dissolved and corroded upon contact with water. The soluble substances went into the immersion solution along with water molecules' movement. Therefore, the pores and fissures became larger and more rounded. In addition, the clay minerals expanded due to water absorption under water-rock interaction. As a result of the expansion stress, stress concentration at the crack tip became more significant, promoting crack initiation and propagation. The mineral particles on the surfaces of new cracks would undergo another round of physical and chemical reactions, including corrosion, dissolution, and water absorption expansion. Such interactions promoted the continuous damage and failure of sandstone. Under the joint action of the above factors, the macromechanical parameters and the energy storage characteristics of sandstone deteriorated as the water content increased.

The performed analysis of the test results revealed that the mechanical parameter deterioration and failure modes of sandstone samples varied with the water content. This implied that the water had varying physical and chemical impacts on sandstone at different stages of water immersion tests. At the initial stage of water immersion, the water-rock interaction was primarily featured by water molecules' absorption onto the mineral particles, which was a physical interaction. The absorption rate was relatively high, and the sandstone strength decreased gradually.

As the water immersion was prolonged, the water content of the sandstone samples became saturated. The water-rock interaction was predominantly the corrosion of mineral particles at this stage, with a progressive enhancement of the chemical reaction. The secondary porosity increased within the sandstone samples under physical actions and chemical reactions. The area of rock-water interaction increased, while the area and degree of bonding between mineral particles decreased. The skeleton of mineral particles was weakened gradually. The sandstone samples became looser and weaker in structure. The brittleness decreased, and the failure mode changed from brittle to ductile.

7. Conclusions

The results obtained made it possible to draw the following conclusions:

(1) As the water content increased, the uniaxial compressive strength, elastic modulus, and elastic energy storage limit decreased gradually in the sandstone samples. Under graded cyclic loading-unloading, the elastic strain during a single cycle increased approximately linearly. As the primary damage, including pores and fissures, accumulated gradually, cyclic loading-unloading curves shifted toward higher strain values. The residual plastic strain first decreased rapidly, then stabilized, and finally showed a minor rise.

(2) Under graded cyclic loading-unloading, the input energy was stored mainly in the form of elastic energy in each cycle; the dissipated energy was primarily spent on overcoming the damping. As the number of cycles increased, the damping energy share first increased gradually and then stabilized. When the normalized number of cycles approached unity, the plastic energy share increased sharply, indicating the ongoing instability failure of the sandstone.

(3) The plastic energy was normalized to plot the damage evolution curve of the sandstone. This curve was subdivided into three stages: decelerated growth, stable accumulation, and accelerated growth. As the water content increased, the slope of the curve of damage factor versus the number of cycles increased gradually at the stage of stable accumulation.

(4) As the water content increased, the pore water exhibited stronger lubrication, wedging, and dissolution effects on mineral particles. As a result, the mineral particles became more rounded. The bonding force between the mineral particles decreased, and the failure mode of sandstone changed from brittle to ductile.

Acknowledgements The authors are grateful to the financial support from the key scientific research project of Shanxi Province (No.57820191101016), the bidding project of Shanxi Province of China (No.20191101016) and the Doctoral Innovation Fund of Anhui University of Science and Technology (No.2021CX1003).

Availability of data and materials The datasets used and/or analysed during the current study are available from the corresponding author on reasonable request.

Declaration

Conflicts of interests The author(s) declare(s) that they have no competing interests.

References

Bian ZF, Zhou YJ, Zeng CL, Huang J, Pu H, Axel P, Zhang BS，Habil CB, Bai HB, Meng QB, Chen N (2021) An discussion of the basic problems for the construction of underground pumped storage reservoir in abandoned coal mines. J China Coal Soc https://doi.org/10.13225/j.cnki.jccs.YG21.0392

Chen GQ, Li TB, Wang W, Zhu ZF, Chen ZQ, Tang OL (2019) Weakening effects of the presence of water on the brittleness of hard sandstone. Bull Eng Geol Environ 78:1471-1483

Fan JY, Xie HP, Jie C, Jiang DY, Li CB, Tiedeu WN, Ambre J (2020) Preliminary feasibility analysis of a hybrid pumped-hydro energy storage system using abandoned coal mine goafs. Applied Energy 258:114007

Geng JS, Cao LW (2020) Failure analysis of water-bearing sandstone using acoustic emission and energy dissipation. Engineering Fracture Mechanics 231:107021

Gu DZ (2015) Theory framework and technological system of coal mine underground reservoir. J China Coal Soc 40:239-246

Hashiba K, Fukui K (2015) Effect of water on the deformation and failure of rock in uniaxial tension. Rock Mech Rock Eng 48:1751-1761

Hua W, Li JX, Dong SM, Pan X (2019) Experimental Study on Mixed Mode Fracture Behavior of Sandstone underWater-Rock Interactions. Processes 7: 70

Jardon S, Ordonez A, Alvarez R, Cienfuegos P, Loredo J (2013) Mine Water for energy and water supply in the central coal basin of Asturias (Spain). Mine Water and the Environment 32(2):139-151

Kuwahara Y, Kyamamoto I, Hirasawa T (1990) An experimental and theoretical study of inelastic deformation of brittle rocks under cyclic uniaxial loading. Tohoku Geophys J 33(1): 1-21

Li TB, Chen ZQ, Chen GQ, Ma CC, Tang OL, Wang MJ (2015) An experimental study of energy mechanism of sandstone with different moisture contents. Rock and Soil Mechanics 36(S2): 229-236 (in Chinese)

Li W, Wang DH, Li HJ (2019) Environmental engineering issues induced by abandoned coal mine hidden disasters. IOP Conference Series:Earth and Environmental Science 237:022039

Liu Y, Dai F, Dong L, Xu NW (2018) Experimental investigation on the fatigue mechanical properties of intermittently jointed rock models under cyclic uniaxial compression with different loading parameters. Rock Mech Rock Eng 51(1): 47-68

Li YH，Jing HW，Zeng QY (2006). Development and application of digital photographic measurement software system for geotechnical engineering. Chinese Journal of Rock Mechanics and Engineering S2:3859-3866(in Chinese)

Ma CQ, Li HZ, Niu Y (2018) Experimental Investigation on the Mechanical Behavior and Damage Evolution Mechanism of Water-Immersed Gypsum Rock. Environmental Earth Sciences 77:23

Niu SJ, Ge SS, Yang DF, Dang Yuan-heng, YU Jin, Zhang Sheng (2018) Mechanical properties and energy mechanism of saturated sandstones. Journal of Central South University 25(6):1447-1463

Pu H, Bian ZF, Zhang JX, Xu JC (2021) Research on a reuse mode of geothermal resources in abandoned coal mines. J China Coal Soc 46(2):677-687

Stevens JL, Holcomb DJ (1980) A Theoretical investigation of the sliding crack model of dilatancy. Journal of Geophysical Research 85(B12):7091-7100

Wong LNY, Maruvanchery V, Liu G (2016) Water effects on rock strength and stiffness degradation. Acta Geotech 11:713-737

Wang H, Yang TH, Liu HL, Zhao YC, Deng WX, Hou XG (2017) Mechanical properties and energy evolution of dry and saturated sandstones under cyclic loading. Rock and Soil Mechanics, 38(6): 1600-1608 (in Chinese)

Xie H, Ju Y, Li L (2005) Criteria for strength and structural failure of rocks based on energy dissipation and energy release principles. Chin J Rock Mech Eng 24:3003–10 (in Chinese)

Xie H, Zhao JW, Zhou HW, Ren SH, Zhang RX (2020) Secondary utilizations and perspectives of mined underground space. Tunnelling and Underground space Technology 96:103129

Yu Y, Tang SB, Tang CA (2019) Experimental study on the influence of water content on instantaneous and creep mechanical properties of red sandstone. J China Coal Soc 44(2):473-481 (in Chinese)

Zhou ZL, Cai X, Cao WZ, Li XB, Xiong C (2016) Influence of Water Content on Mechanical Properties of Rock in Both Saturation and Drying Processes. Rock Mech Rock Eng 49:3009-3025

Fig. 1. Sandstone samples with different water contents

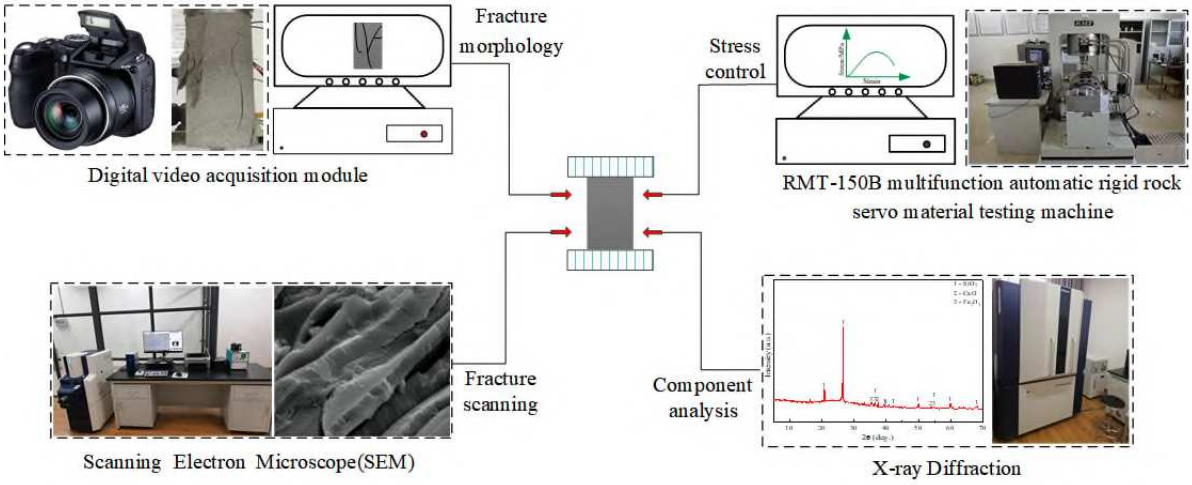

Fig. 2. Test system

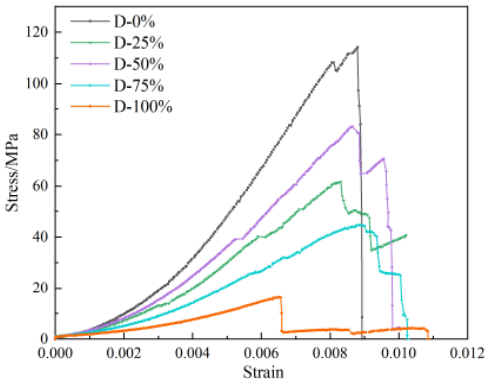

Fig. 3. Stress-strain curve under uniaxial loading

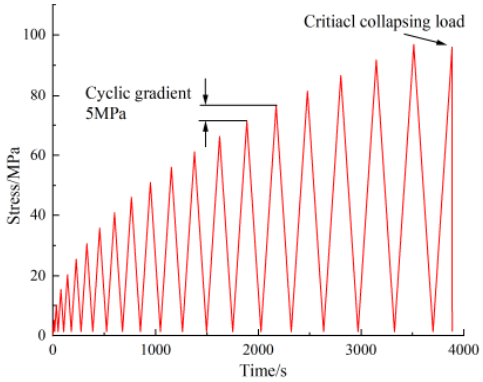

Fig. 4. Stress path of the cyclic loading-unloading test

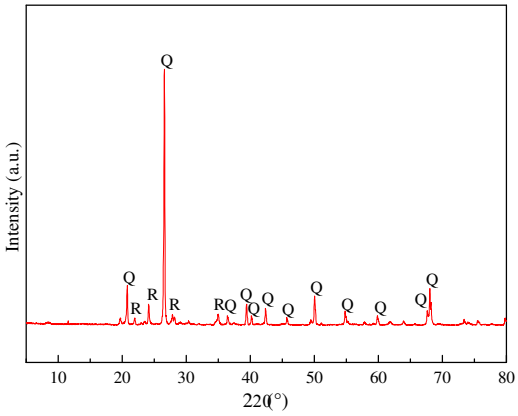

(a) Water content of 0%

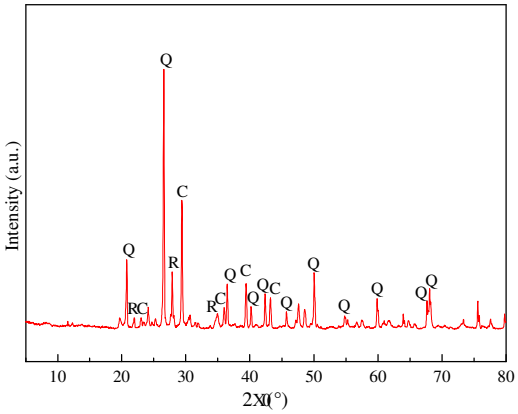

(b) Water content of 1.01%

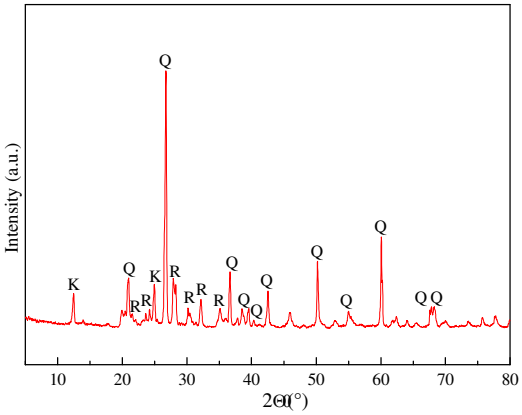

(b) Water content of 2.07%

Fig. 5. XRD patterns of sandstone samples

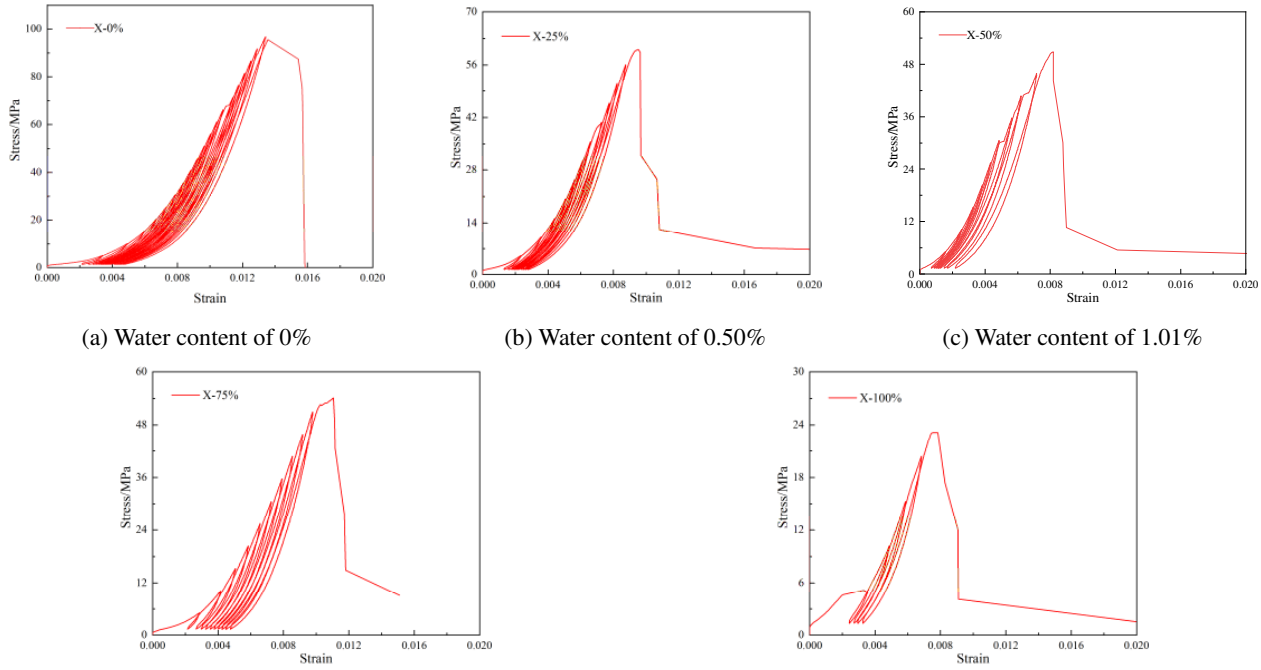

(a) Water content of 0%

(b) Water content of 0.50%

(c) Water content of 1.01%

(d) Water content of 1.52%

(e) Water content of 2.07%

Fig. 6. Cyclic stress-strain curves

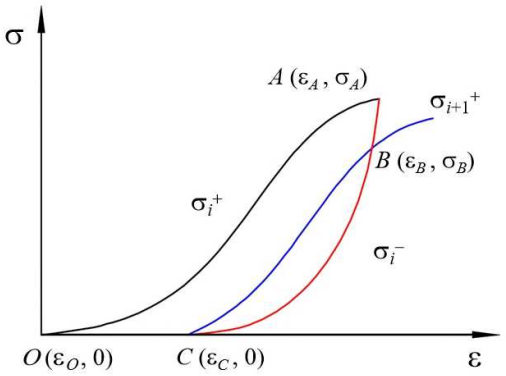

Fig. 7. Stress path of cyclic loading-unloading

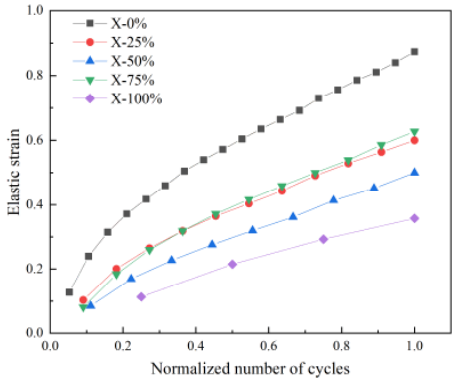

(a) Elastic strain

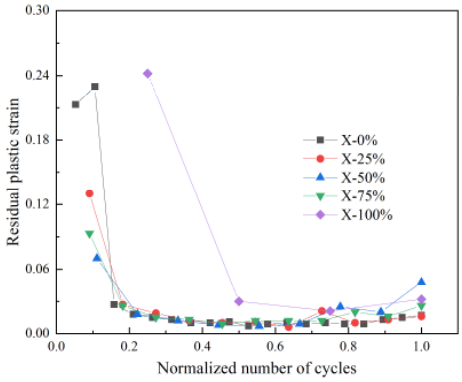

(b) Plastic strain

Fig. 8. Elastic strain and plastic strain curves

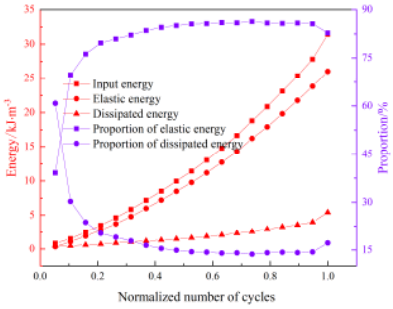

(a) Water content of 0%

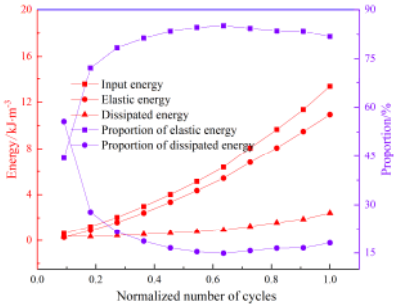

(b) Water content of 0.50%

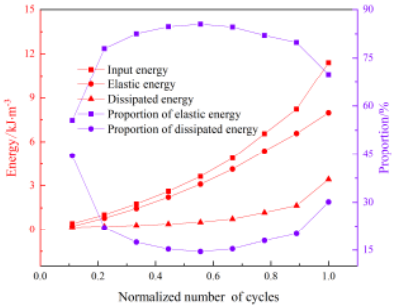

(c) Water content of 1.01%

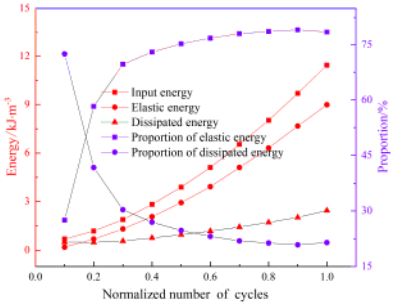

(d) Water content of 1.52%

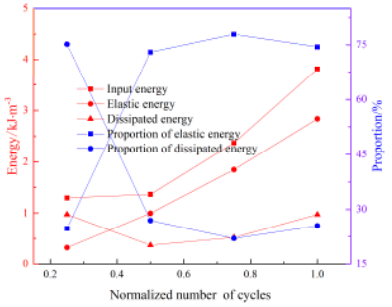

(e) Water content of 2.07%

Fig. 9. Energy distribution diagram

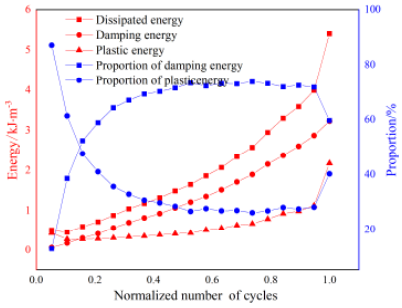

(a) Water content of 0%

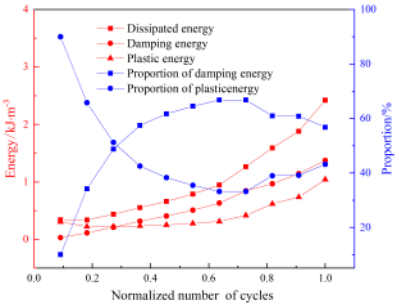

(b) Water content of 0.50%

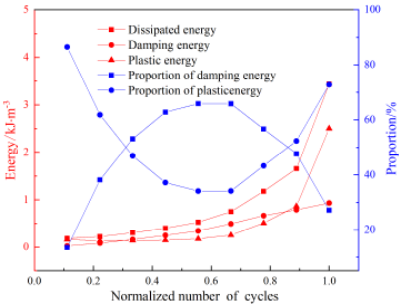

(c) Water content of 1.01%

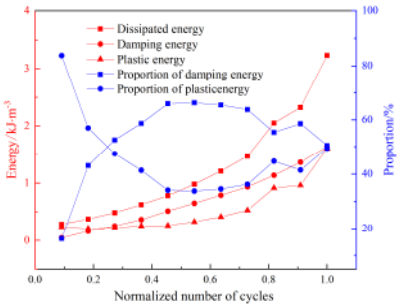

(d) Water content of 1.52%

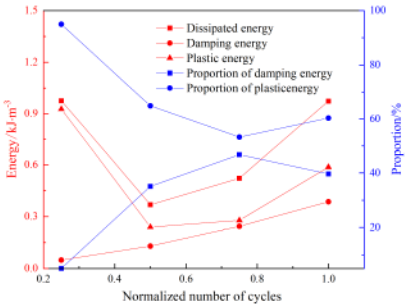

(e) Water content of 2.07%

Fig. 10. Dissipated energy distribution diagram

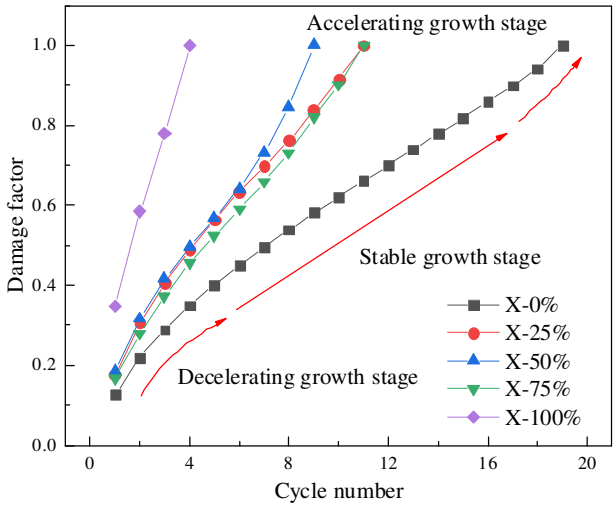

Fig. 11. Damage evolution curve

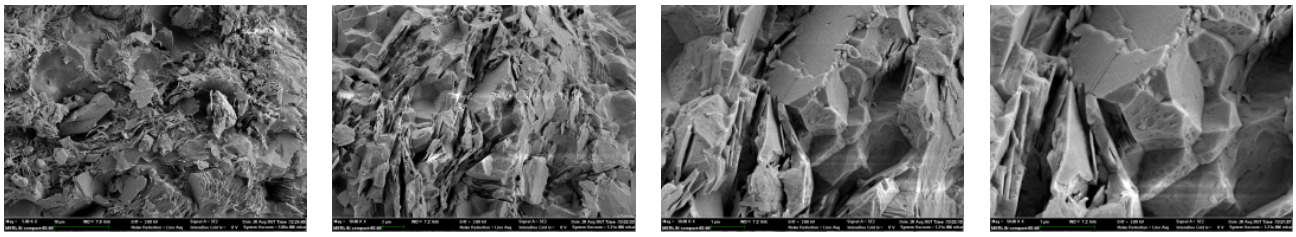

Magnification 5000 x Magnification 10000 x Magnification 30000 x Magnification 50000 x

(a) Dry state

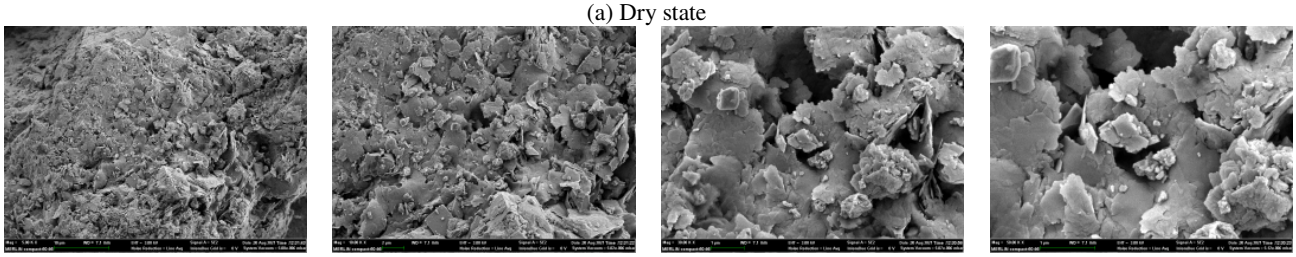

Magnification 5000 x Magnification 10000 x Magnification 30000 x Magnification 50000 x

(b)Semi-saturated state

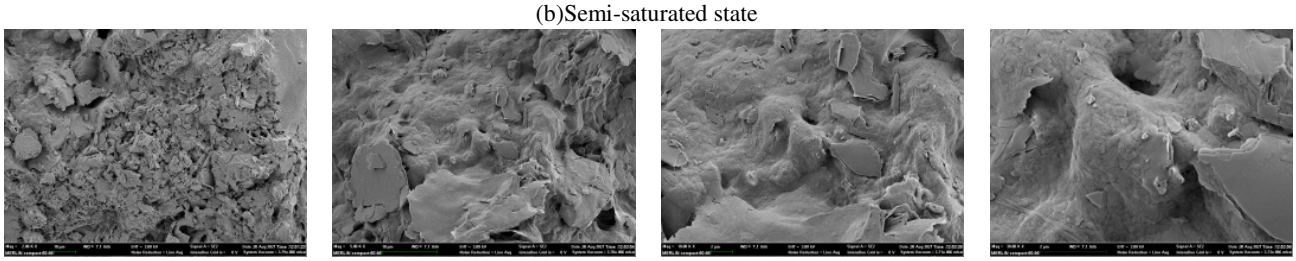

Magnification 2000 x Magnification 5000 x Magnification 10000 x Magnification 30000 x

(c) Saturated state

Fig.12. Microstructural characteristics of sandstone samples

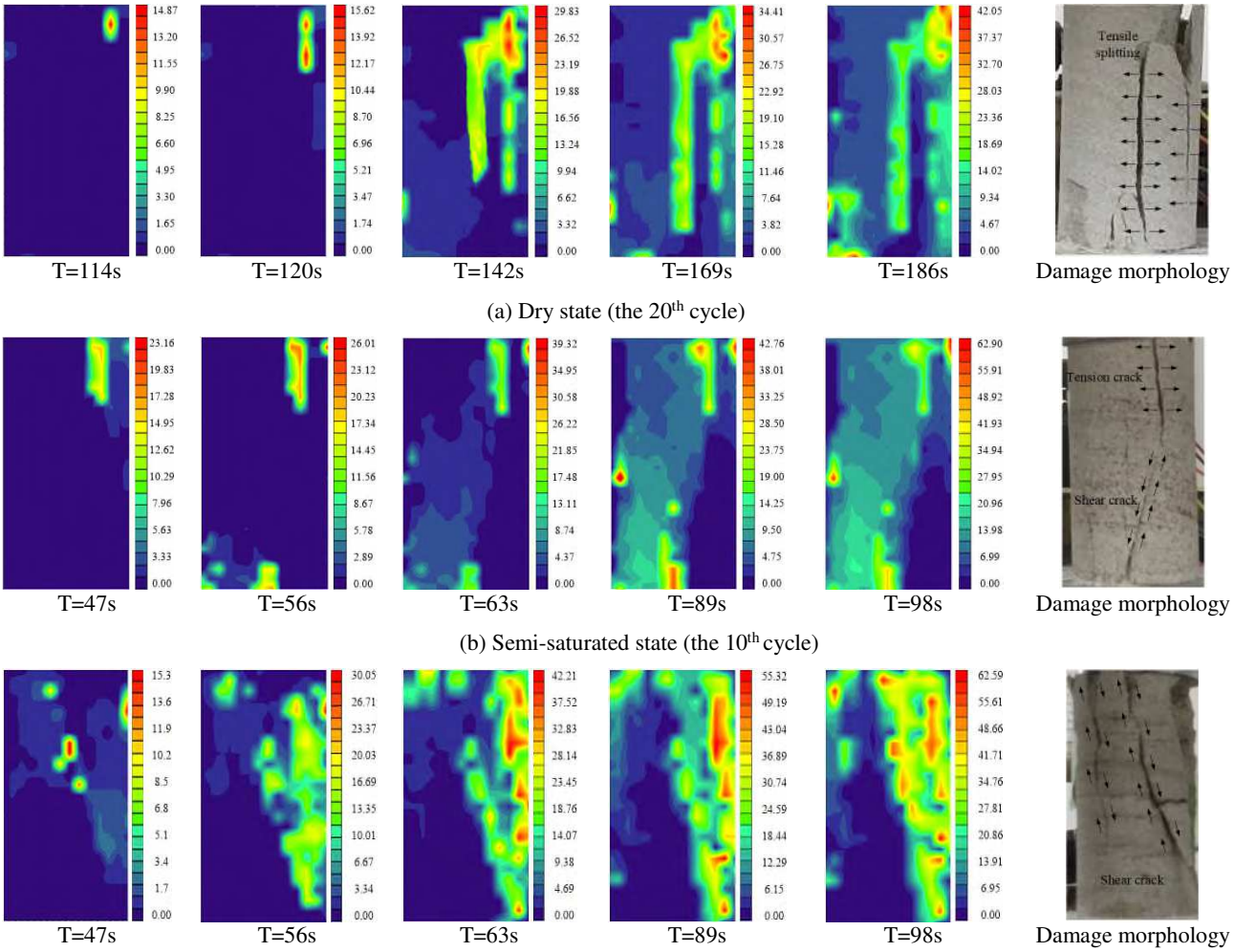

Fig. 13. Cloud maps of sandstone displacement field with different water contents under graded cyclic loading-unloading conditions

Table 1. Mechanical parameters under different water contents

Sample No.	Water content/%	Uniaxial compressive strength/MPa	Elastic modulus/GPa	Poisson's ratio	Softening coefficient
D-0	0.00	114.09	19.70	0.11	1
D-25	0.50	83.12	13.91	0.16	0.73
D-50	1.01	61.52	10.58	0.21	0.54
D-75	1.52	44.47	6.21	0.26	0.39
D-100	2.07	16.39	3.47	0.31	0.14